Plasma Phys. Control. Fusion **45** (2003) 469–487 PII: S0741-3335(03)58124-6

Laboratory characterization of an imaging reflectometer system

T Munsat[1], E Mazzucato[1], H Park[1], C W Domier[2], N C Luhmann Jr[2], A J H Donné[3] and M van de Pol[3]

[1] Plasma Physics Laboratory, Princeton University, PO Box 451, Princeton NJ 08543, USA
[2] University of California, Davis CA 95616, USA
[3] FOM-Instituut voor Plasmafysica Rijnhuizen, Postbus 1207, NL-3430 BE Nieuwegein, The Netherlands

E-mail: tmunsat@pppl.gov

Received 10 January 2003, in final form 26 February 2003
Published 25 March 2003
Online at stacks.iop.org/PPCF/45/469

Abstract
While microwave reflectometry has proven to be a sensitive tool for measuring electron density fluctuations in many circumstances, it has also been shown to have limited viability for core measurements and/or conditions of strong turbulence. To this end, a new instrument based on two-dimensional imaging reflectometry has been developed to measure density fluctuations over an extended plasma region in the TEXTOR tokamak. Laboratory characterization of this instrument has been performed using corrugated reflecting targets as an approximation to plasma reflections including two-dimensional turbulent fluctuations of various magnitude and poloidal wavenumber. Within this approximation, the imaging reflectometer can recover the spectral and spatial characteristics of the reflection layer lost to or otherwise inaccessible to conventional techniques.

1. Introduction and background

Microwave reflectometry has been extensively employed in tokamak plasmas for the detection of turbulence, due to its relatively simple implementation and its high sensitivity to small perturbations of electron density. Despite its widespread and long-standing use, however, the interpretation of reflectometry data from fluctuations remains an outstanding issue, due to the effects of interference betweeen components of the reflected waves [1, 2].

For the simple case of one-dimensional fluctuations (radial only), it has been shown that the fluctuating component of the signal phase is given by the approximation of geometric optics [3]

$$\tilde{\phi} = k_0 \int_0^{r_c} \frac{\tilde{\varepsilon}(r)}{\sqrt{\varepsilon_0}}\, \mathrm{d}r, \tag{1}$$

as long as the radial fluctuation wavenumber satisfies the condition $k_r < k_0/(k_0 L_\varepsilon)^{1/3}$, where $L_\varepsilon = (\mathrm{d}\varepsilon_0/\mathrm{d}r)^{-1}_{r=r_\mathrm{c}}$ is the scale length of the plasma permittivity at the plasma cutoff $r = r_\mathrm{c}$ and k_0 is the wavenumber of the probing beam.

Within this approximation, the power spectrum of $\tilde{\phi}$ as a function of the power spectrum of the density fluctuations is given by

$$\Gamma_\phi(k_r) = \pi M \frac{k_0^2 L_n}{|k_r|} \Gamma_n(k_r), \tag{2}$$

where $L_n = n/(\mathrm{d}n/\mathrm{d}r)_{r=r_\mathrm{c}}$ is the scale length of the electron density n, $M \equiv (n\mathrm{d}\varepsilon/\mathrm{d}n)_{r=r_\mathrm{c}}$ ($\approx$1 for the ordinary mode and $\approx$2 for the extraordinary mode), $\Gamma_\phi(k_r)$ is the power spectrum of the measured $\tilde{\phi}$ (considered to be a function of r_c), and $\Gamma_n(k_r)$ is the power spectrum of the relative plasma density fluctuation $\tilde{n}/n$ [1].

In the presence of two-dimensional turbulent fluctuations, the interpretation of reflectometry becomes considerably more complex. Unfortunately, this is precisely the case of interest for tokamak plasmas, which exhibit both radial and poloidal fluctuations. The difficulty arises from the fact that when the plasma permittivity fluctuates perpendicularly to the direction of propagation of the probing wave, the spectral components of the reflected field propagate in different directions. This can result in a complicated interference pattern on the detector plane, from which it is difficult to extract any information about the plasma fluctuations. In essence, the measurement of the fluctuations is limited by the fluctuations themselves.

Some authors have taken these phenomena into account by expressing an upper-bound on the measurable fluctuation levels in particular experiments [4]. Additionally, various techniques have been employed to account for the effects of two-dimensional turbulence, at least for moderate fluctuation levels. In one such technique, algebraic correction factors based on knowledge of the fluctuation amplitude and/or poloidal spectrum are used to relate measured signal correlation lengths to inferred fluctuation correlation lengths [5]. In another method, the reflectometer signals are adjusted by numerically back-projecting the measured complex electric fields through the modelled dispersive plasma medium, providing a correction to the field distribution [6]. In the limit of strong fluctuations, however, the signal can become distorted beyond repair even by advanced numerical techniques.

The study of the effect of two-dimensional turbulence on reflectometer measurements, both on TFTR and in a series of numerical simulations, led to the development of the microwave imaging reflectometry (MIR) concept [3, 7, 8]. In this technique, large-aperture optics at the plasma edge are used to collect as much of the scattered wavefront as possible and optically focus an image of the cutoff layer onto an array of detectors, thus restoring the integrity of the phase measurement. A detailed description of the MIR technique is provided in [7, 8].

The goal of the MIR technique is to provide a method of fluctuation measurement that relies as little as possible on *a priori* knowledge of the plasma parameters, in particular the poloidal wavenumber (k_θ) spectrum and the fluctuation amplitude ($\Delta\phi$). The set of phase measurements taken at individual points along a cutoff surface provide a 'snapshot' of the cutoff at each sampled moment, which can then be evolved in time to provide spectra in both space and time. While the advantage of this technique is that it does not require extensive computation or modelling to interpret the results, this technique is itself limited by the use of large optics. While conventional reflectometry configurations can launch and receive waves over a great variety of positions in the plasma (provided the return waves are uncorrupted by interference), the MIR technique is limited to probing plasmas with the cutoff within the depth-of-field of the optics (typically within 5–10 cm of the nominal focal position). This is similar to a standard camera lens, which also trades off collection aperture for focal depth-of-field.

An important result from the numerical simulations in [3] which is critical to the implementation of the MIR technique is the demonstration of a 'virtual cutoff' surface, located behind the actual cutoff surface, from which the reflected waves appear to have originated (to an observer at the plasma edge). The location of the virtual cutoff can be heuristically described as the intersection of the asymptotes of the ray trajectories of the probing wave before and after reflection, shown schematically in figure 1. If the reflected rays are collected by a large-aperture optical system with its object-plane located at the virtual cutoff, the spatial structure of the density fluctuations at the actual cutoff layer can be determined by the detected phase at the image plane.

The distance between the actual and virtual cutoff layers was calculated to lowest order for planar geometry in [7], and is given by

$$\Delta r \approx \int_{r_c}^{r_b} \frac{1 - \sqrt{\varepsilon(r)}}{\sqrt{\varepsilon(r)}}\, \mathrm{d}r. \tag{3}$$

A practical approximation for this distance has been calculated for cylindrical geometry, as a function of the radius of the cutoff surface r_c and the scale length of the plasma permittivity L_ε at the cutoff:

$$\Delta r \approx a\, L_\varepsilon^{\mathrm{b}}, \tag{4}$$

where $a = 1-0.89\exp(-0.43r_c)$, $b = 1-0.66\exp(-0.45r_c)$, and all dimensions are in metre. To derive this expression, the virtual cutoff was calculated over the range $0.01\ \mathrm{m} \leqslant L_\varepsilon \leqslant 0.5\ \mathrm{m}$ and $0.1\ \mathrm{m} \leqslant r_c \leqslant 5.0\ \mathrm{m}$. The density scale-length near $r = r_c$ was imposed by using the form $\varepsilon(r) = \mathrm{erf}((r-r_c)/L_\varepsilon)$ where $\mathrm{erf}(x) \equiv 2/\pi \int_0^x \exp(-t^2)\,\mathrm{d}t$ is the error function (this form was chosen because it is linear near the cutoff, and smoothly approaches unity as $r \to \infty$). For TEXTOR parameters of $r_c = 0.3$ m and $L_\varepsilon = 0.4$ m, this results in $\Delta r \approx 15$ cm.

A MIR instrument of this type has been developed for the TEXTOR tokamak. The details of this instrument are presented in a separate paper [9], and only a brief overview is outlined here. In the TEXTOR instrument, shown in figure 2, the primary focusing optical set is comprised of two large cylindrical mirrors, arranged to tailor the illumination beam wavefront to match the toroidal cutoff surface. The MIR system has been combined with an electron cyclotron emission imaging diagnostic [10], which shares the 42 cm $\times$ 20 cm vacuum window and large front-end optics, enabling simultaneous measurement of $\tilde{n}_e$ and $\tilde{T}_e$ fluctuations in the same plasma volume.

The TEXTOR MIR instrument, installed initially at a fixed-frequency of 88 GHz, covers a $\lesssim$15 cm poloidal region of the cutoff surface with a spatial resolution of $\sim$1 cm, leading to a theoretical k_θ resolution of $0.4\ \mathrm{cm}^{-1} \leqslant k_\theta \leqslant 3\ \mathrm{cm}^{-1}$. It is important to specify the distinction between making reflectometric measurements in the presence of poloidal fluctuations and

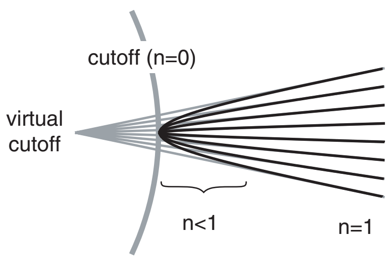

Figure 1. Heuristic description of the virtual cutoff layer. Rays refract near the plasma cutoff layer ($n < 1$), reaching a turning point at the cutoff ($n = 0$). The ray asymptotes meet at a common location, where, to an outside observer, the radiation appears to have originated.

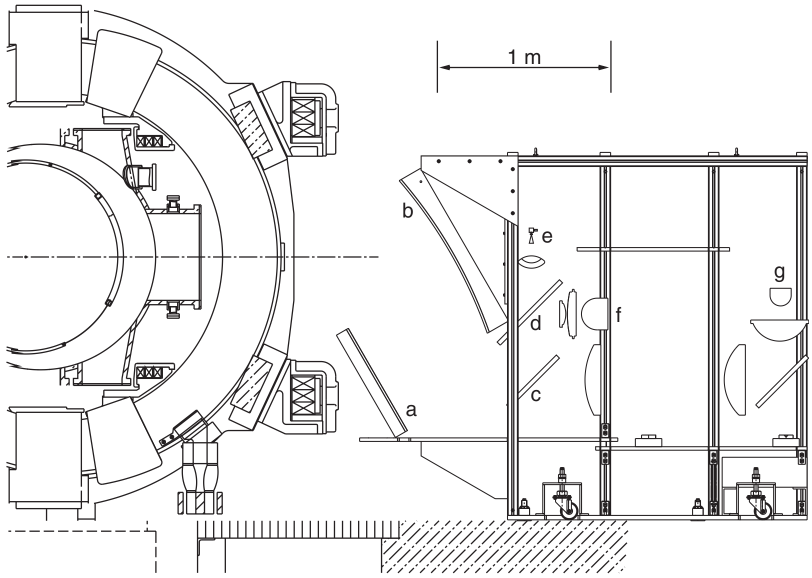

Figure 2. TEXTOR poloidal cross-section with the MIR/ECEI combined system.

making reflectometric measurements of the poloidal fluctuations. While the majority of this paper focuses on the validity of measurements in the presence of poloidal fluctuations, in fact the MIR project represents the first use of simultaneous, localized reflectometry measurements to produce a time-resolved mapping of k_θ. With this in mind, the stated k_θ resolution of the TEXTOR MIR system refers to that which can actually be resolved by the instrument. Measurements can be made in the presence of arbitrarily low k_θ, down to $0\,\mathrm{cm}^{-1}$.

In this paper we explore the issue of reflectometry interpretation through the experimental characterization of the TEXTOR imaging reflectometer. Namely, we present a series of experiments which test the response of the MIR instrument to an approximation of a fluctuating plasma cutoff. As part of this paper, we also demonstrate the point of failure of one-dimensional reflectometry in this approximation and the recovery of phase data through two-dimensional imaging using the TEXTOR MIR instrument, as well as the capability of the imaging reflectometry technique to recover poloidally localized phase information for quantitative determination of poloidal spatial mode structure.

Sections 2 and 3 contain a description of the experiments, which were used to assess the performance of the TEXTOR MIR instrument. Section 4 presents a series of calculations relating to the target–reflector experiments, which illustrate the primary dependences of the experimental results. Section 5 presents an exploration of the impact of these findings to correlation-length measurements. A discussion of the results follows in section 6.

2. Characterization of the TEXTOR MIR instrument

A laboratory characterization of the TEXTOR MIR instrument was performed using corrugated reflecting targets of known shape to simulate the fluctuating plasma reflection layer. It has been previously shown that the reflected wavefield from a plasma cutoff exhibiting two-dimensional random fluctuations resembles the reflection of waves from a rough surface [3, 11]. Under conditions in which this approximation is valid, reflection from a corrugated mirror provides a first test of the instrument response to a fluctuating reflection layer.

For the initial tests of the MIR configuration for a single point measurement (i.e. section 2), the apparatus was set up as shown in figure 3(*a*), with a Gaussian launching horn, steering and focusing optics, and a simple rectangular receiver horn. For multipoint measurements (i.e. section 3), the receiver horn was replaced with the 16-element TEXTOR detector array.

This study also included a performance characterization of a conventional reflectometer arrangement, consisting of a Gaussian launching horn and a simple detector horn with no imaging optics, also arranged to measure the reflected signals from the corrugated targets. This type of target-reflector arrangement has been used in the past to simulate doppler-shift measurements of poloidal rotation with reflectometry [12], and even to investigate the effects of two-dimensional fluctuations on reflectometry measurements [13], though in the latter case only the effects on total collected power using a one-dimensional configuration were considered.

The laboratory arrangements of the MIR and one-dimensional configurations are schematically shown in figures 3(*a*) and (*b*), respectively. The target reflectors were constructed from an inner wheel 60 cm in diameter and 20 cm wide, with a sinusoidally corrugated flexible aluminium strip wrapped around the circumference. The corrugation wavelength λ_{corr} (labelled $2\pi/k_\theta$ in figure 3) and corrugation height (labelled h_{corr}) were both precisely imposed upon construction via the spacing and height difference of alternating high and low shims supporting the flexible outer surface.

Measurements were taken with each of the reflectometer systems for a series of targets covering a range of k_θ and h_{corr}, and for geometries covering a range of distances from the instrument to the target surface. This distance, labelled d in figure 3, is defined as the distance between the target surface to the first mirror in the case of the MIR system, and as the distance between the target surface and the launch/receive horns in the case of the one-dimensional system. The focal distance of the MIR system $d_0 \equiv d$ (image focus) is 235 cm. For each configuration, the measurement was taken by simply spinning the target wheel and collecting a time-trace of the quadrature signals from the reflectometry system.

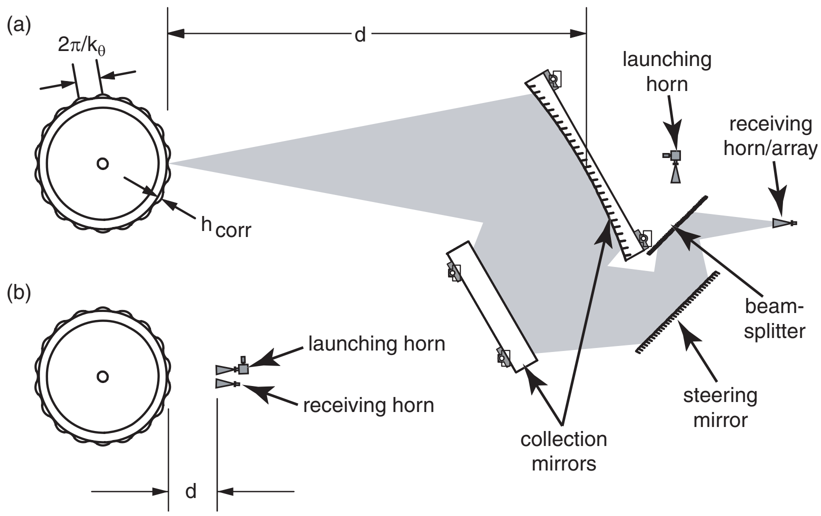

Figure 3. Schematic illustration of the characterization test set-up, showing the MIR and one-dimensional configurations ((*a*) and (*b*), respectively). The target reflectors were constructed with various imposed values of corrugation wavelength (labelled $2\pi/k_\theta$) and corrugation height (labelled h_{corr}). Measurements were taken over a range of separation distances d.

In order to form a reference measurement to which the reflectometer measurements could be compared, each target surface was independently measured using Leica 'Laser Tracker' [14], a visible-laser interferometer with 10 μm precision.

A result from this off-line study is shown in figure 4, in which the measurements from the one-dimensional and MIR systems are compared to the reference measurement. The target in this case had corrugations of $k_\theta = 1.25\,\mathrm{cm}^{-1}$ and depth $\approx 1.7\,\mathrm{mm} = \lambda_0/2$, where λ_0 is the wavelength of the probing microwave beam, leading to a nominal phase fluctuation of $\Delta\phi \approx 2\pi$. Using equation (2) and nominal TEXTOR parameters of $L_n = 46\,\mathrm{cm}$ and $k_r = 1.0\,\mathrm{cm}^{-1}$, this corresponds to $\langle\tilde{n}_e\rangle/n_e \approx 1\%$. In the figure, the grey curves represent the reference measurement of the corrugation shape scaled by $4\pi/\lambda_0$, corresponding to the ideal phase shift induced on the reflected beam. The black curves represent the reflectometer measurements.

Figures 4(*a*) and (*b*) correspond to measurements taken with the one-dimensional system at distances of 10 cm and 30 cm, respectively. Figure 4(*c*) corresponds to a measurement taken with the MIR system located at d_0, at the focal distance of 235 cm.

Clearly from figure 4(*a*), the one-dimensional configuration produces a close match to the reference curve, although it appears that some minor level of interference has reduced the measured level of phase modulation compared to the actual surface. Despite this, the

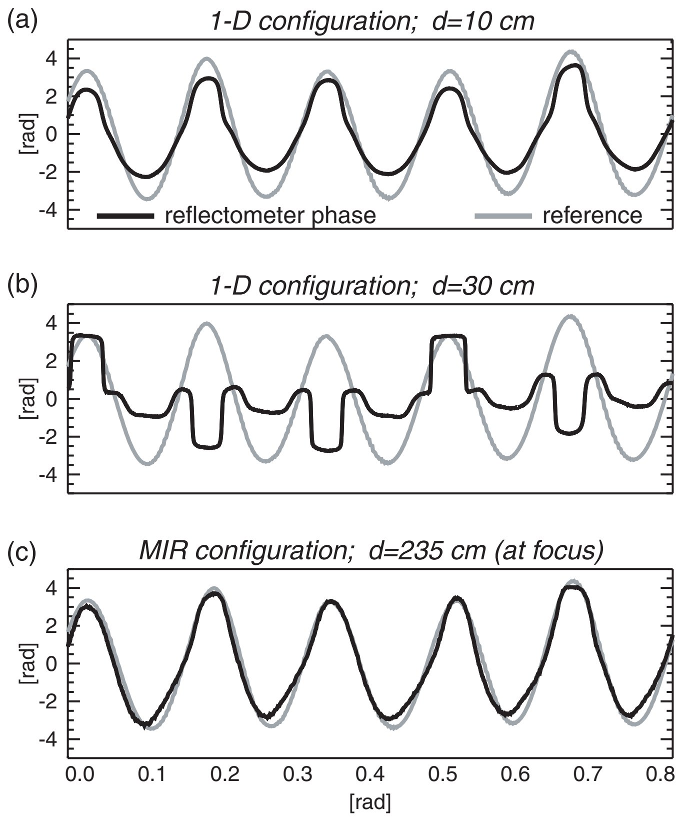

Figure 4. Waveforms from the one-dimensional system (*a*), (*b*) and MIR system (*c*), from measurements of a target reflector having corrugations of $k_\theta = 1.25\,\mathrm{cm}^{-1}$ and depth $\approx$1.7 mm, leading to $\Delta\phi \approx 2\pi$.

majority of the spectral power is contained in the fundamental k_θ of the target wheel. The one-dimensional measurement at 30 cm (figure 4(*b*)), however, is quite distorted, no longer representing the target surface. Clearly a significant fraction of the spectral power in this plot is contained in higher harmonics of k_θ, and the target shape (representing the fluctuations at the plasma cutoff), cannot be inferred from the reflectometer data in this case. It should be pointed out that this experiment represents a simplified case of one single poloidal mode, chosen to illustrate the effect of two-dimensional fluctuations in the simplest possible manner. The inclusion of a more realistic spectrum containing many modes would distort the measured pattern even further (depending, of course, on the shape and magnitude of the k_θ spectrum), and is revisited in sections 4 and 5.

The MIR waveform (figure 4(*c*)) represents the cleanest measurement of the wheel surface, despite being physically the furthest removed from the target. Even the small irregularities in the reference curve (due to construction irregularities in the target wheel) are accurately reproduced by the MIR instrument.

In order to quantify the degree to which the reflectometer measurements accurately reproduce the reference surface, the cross-correlation coefficient ρ_{XY} was calculated between the power spectra of the reflectometer and reference curves for measurements over a wide range of d, the distance between the instrument and the target surface. The cross-correlation coefficient is defined in the standard way (e.g. [15]):

$$\rho_{XY} = \frac{R_{XY}}{\sqrt{R_{XX} R_{YY}}}, \tag{5}$$

where the cross-correlation function $R_{XY} \equiv \int X(k)Y(k)\,\mathrm{d}k$, and in this case $X(k) \equiv [\int \phi_{\mathrm{ref}}(t)\mathrm{e}^{\mathrm{i}kt}\,\mathrm{d}t]^2$ is the power spectrum of the reference curve and $Y(k) \equiv [\int \phi_{\mathrm{data}}(t)\mathrm{e}^{\mathrm{i}kt}\,\mathrm{d}t]^2$ is the power spectrum of the reflectometer measurement. These data, plotted for both the one-dimensional and MIR systems, are shown in figure 5(*a*). In the figure, triangles represent the one-dimensional measurements, and squares represent the MIR measurements.

For the one-dimensional case, the correlation is nearly unity for $d = 10$ cm, and falls sharply as the distance is increased to 30 cm or more. As was seen in figure 4(*b*), measurements at or beyond 30 cm no longer represent the actual surface, demonstrated by the $\leqslant 0.5$ cross-correlation figure. Interestingly, after reaching a minimum value of ≈ 0.05, the cross-correlation figure increases to nearly 0.5 at distances between 60 and 90 cm. This is interpreted as a spurious effect based on the simplicity/periodicity of the target, and can be qualitatively observed in figure 4(*b*). While the waveform in figure 4(*b*) does not represent the actual surface, it does exhibit some degree of periodicity in common with the surface, which gives rise to the finite cross-correlation. In a more realistic configuration including two or more poloidal wavenumbers, this periodicity is broken, and the cross-correlation would remain low in the region of wave interference. This situation is specifically addressed in section 4.

The MIR values are similarly near-unity in the vicinity of the MIR focus, falling off at $d \approx \pm 10$ cm with respect to the focal plane location. This 20 cm range represents the distance over which multi-radial (multi-frequency) data could be collected simultaneously with a fixed set of imaging optics. This plot serves to illustrate the fundamental advantage of the MIR technique, which is that the ‘proximity focusing’ of the one-dimensional system for data taken immediately next to the reflecting surface is transferred to a remote focal plane, physically accessible to a detection system. In this case, the MIR data are taken with the instrument at a distance of over 200 cm from the reflecting surface, in exactly the configuration used for TEXTOR measurements.

Plotted in figure 5(*b*) is the mean absolute deviation of the amplitude, expressed as a fraction of the mean amplitude. These data are important only as a corroboration of the

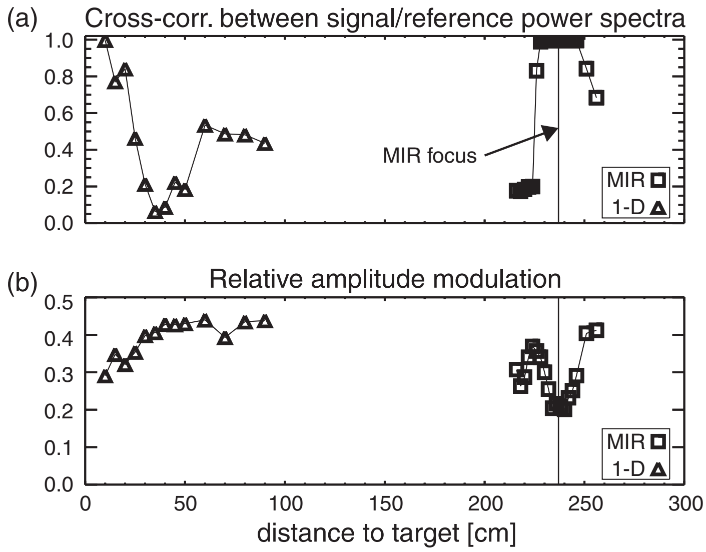

Figure 5. (*a*) Cross-correlation between the reflectometer and reference power spectra for target reflector with $k_\theta = 1.25\,\text{cm}^{-1}$ and $\Delta\phi \approx 2\pi$, plotted for both the one-dimensional (Δ) and MIR ($\square$) configurations. (*b*) Relative amplitude modulation for each reflectometer measurement.

data from figure 5(*a*), with the implication that phase distortion is generally accompanied by strong amplitude modulation of the reflected signal, both of which are direct consequences of wave interference. The most notable feature of this plot is the MIR data, which exhibit a suppression of amplitude fluctuations at the focal point. At the minimum, the fluctuations are $\sim$20%. For the one-dimensional case, the minimum fluctuation level is $\sim$30%, increasing to 40% or more for $d > 50\,\text{cm}$. Ideally, the modulation level would drop to zero at the focal location. The minimum modulation in this case is nonzero due to imperfections in the focal quality of the optical set, as well as the fact that in any real optical system, only a finite solid-angle of the reflected radiation is collected. It should be noted that a higher quality mirror set (to be used in the identical configuration) is being constructed for the TEXTOR installation.

Similar data were taken for a target reflector with identical $k_\theta = 1.25\,\text{cm}^{-1}$ but with $\sim$50% lower corrugation depth ($\Delta\phi \approx 1.3\pi$), and are shown in figure 6. Figures 6(*a*) and (*b*) represent measurements taken with the one-dimensional system at $d = 10\,\text{cm}$ and 95 cm, respectively, and (*c*) represents measurements taken with the MIR system at the focal plane. A notable difference between figures 4(*b*) and 6(*b*) is that the former was recorded at $d = 30\,\text{cm}$ while the latter was recorded at $d = 95\,\text{cm}$. The cross-correlation between the power-spectra is plotted in figure 6(*d*).

Clearly from the waveforms and the correlation plots, the response of both the one-dimensional and MIR systems is improved over the previous case. Both reflectometry configurations exhibit near-unity cross-correlation between the measured and reference power spectra, indicating that for these conditions, the measurement of fluctuations approaches the one-dimensional problem, and is relatively free from interference effects. Indeed, for the case of figure 6, the need for imaging is largely eliminated. The only data point to exhibit significant decorrelation from the reference curve is the measurement at $d = 100$ cm, which contains a high percentage of phase-ambiguities which result in spurious phase excursions in the waveform reconstruction. Relative to the other cases considered here, however, this effect is only observed at quite a large distance from the target.

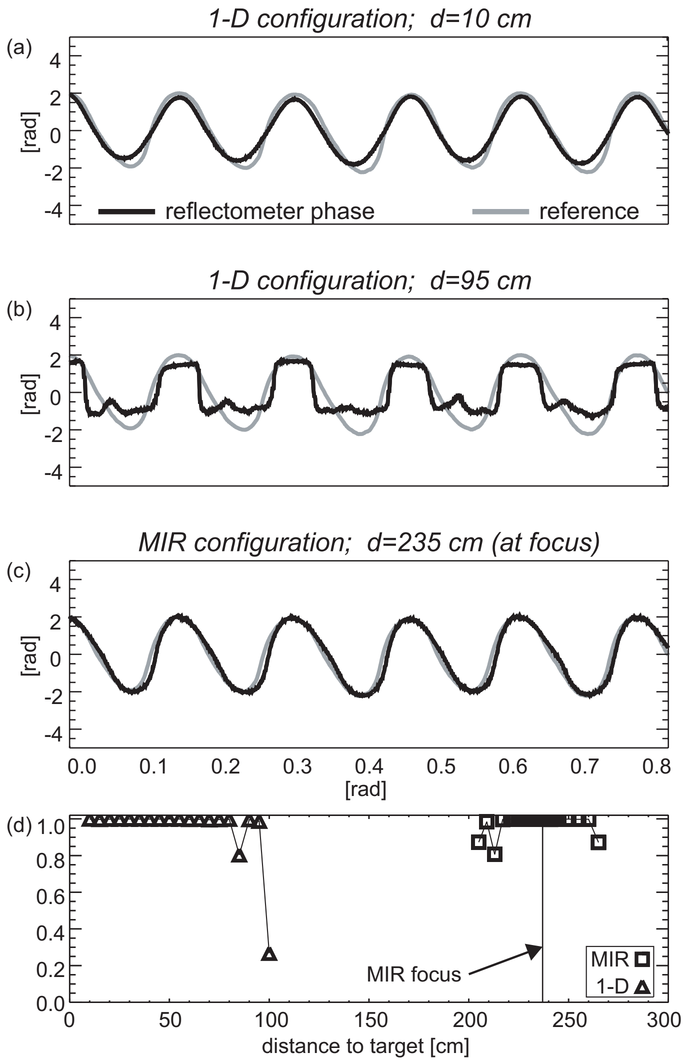

Figure 6. Measurements from the one-dimensional system (*a*), (*b*) and MIR system (*c*) of a target reflector having $k_\theta = 1.25\,\text{cm}^{-1}$ and $\Delta\phi \approx 1.3\pi$. Correlation comparison versus target distance for both configurations (*d*).

Data were also collected for a target reflector with $k_\theta = 2.5\,\text{cm}^{-1}$, higher than the preceding two targets by a factor of 2, and corrugation depth leading to $\Delta\phi \approx 0.7\pi$, somewhat lower than either of the preceding two targets. Data from this target are shown in figure 7. Figures 7(*a*) and (*b*) represent measurements taken with the one-dimensional system at $d = 10$ cm and 25 cm, respectively, and (*c*) represents measurements taken with the MIR system at the focal plane. Again, it should be emphasized that figure 7(*b*) was recorded at $d = 25$ cm, which represents the furthest distance that a coherent waveform was obtained, but is closer than the distances presented in figures 4(*b*) and 6(*b*). The cross-correlation between the power-spectra is plotted in figure 7(*d*).

Clearly, the data from this target are degraded by comparison to the previous targets with lower k_θ. For both the one-dimensional system and the MIR system, the optimum waveform

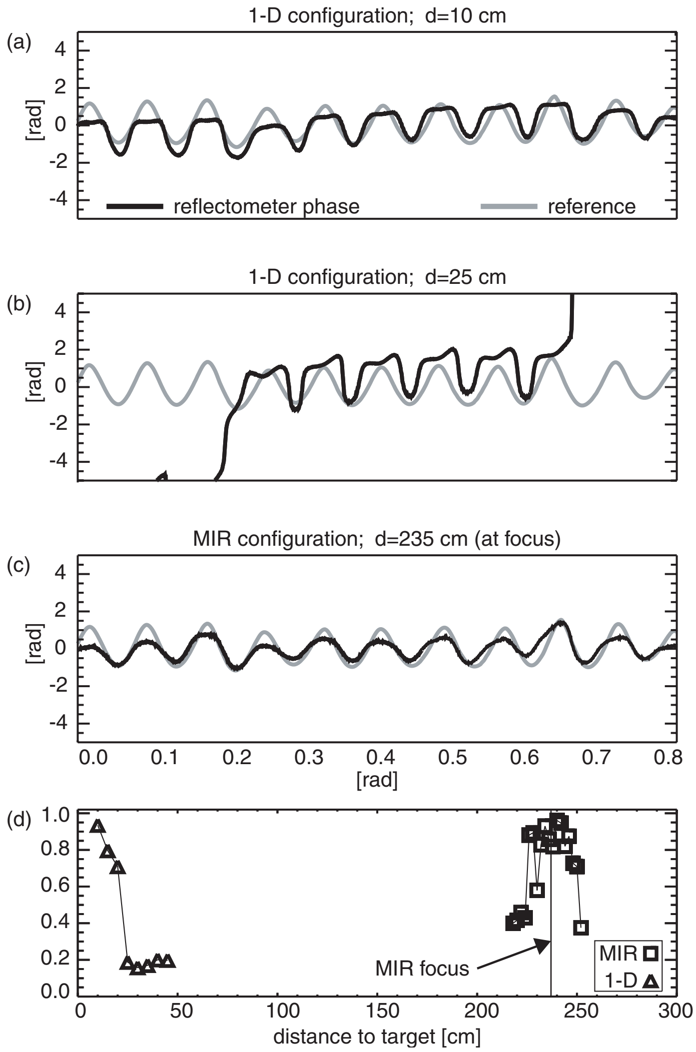

Figure 7. Measurements from the one-dimensional system (*a*), (*b*) and MIR system (*c*) of a target reflector having $k_\theta = 2.5\,\mathrm{cm}^{-1}$ and $\Delta\phi \approx 0.7\pi$. Correlation comparison versus target distance for both configurations (*d*).

(figures 7(*a*) and (*c*), respectively) is perceptibly different from the reference. Additionally, the 'depth of field' of acceptable levels of cross-correlation is reduced for both configurations. As in the previous cases, the similarity between the focal depth of the one-dimensional system and the MIR system is apparent, though the MIR focal plane is transferred away from the target surface. As will be discussed in section 4, reflectometer signal quality in the non-imaged case can degrade very quickly as k_θ is increased.

3. Multipoint measurements to resolve poloidal wavenumber

Measurements of the poloidal wavenumber of the target reflectors were taken by simultaneously recording multiple localized MIR signals as the target was spun through the focal plane.

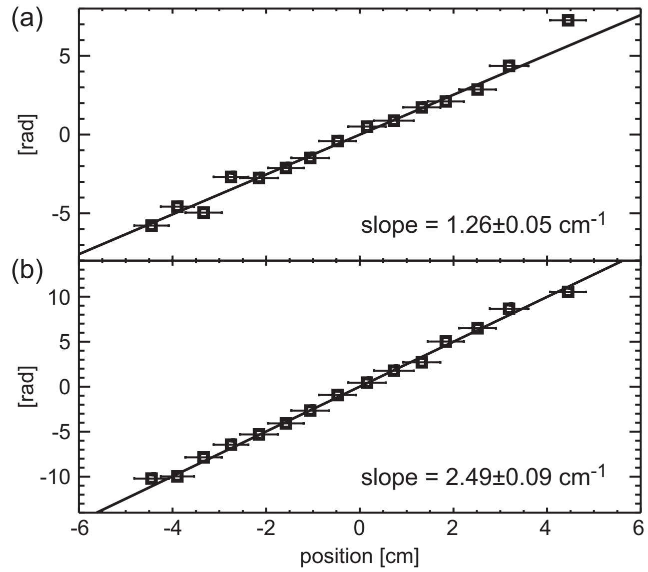

Figure 8. Multipoint measurements of target reflectors to determine poloidal wavenumber. (a) Phase versus position for target having $k_\theta = 1.25\,\mathrm{cm}^{-1}$ and $\Delta\phi \approx 1.3\pi$. ($b$) Phase versus position for target having $k_\theta = 2.5\,\mathrm{cm}^{-1}$ and $\Delta\phi \approx 0.7\pi$. The slope of each data set successfully recovers the poloidal wavenumber to well within the instrumental uncertainty.

The relative phase of each sinusoidal signal was then plotted against the location of each channel, with the measured k_θ of the target determined by the slope of these points.

The results of this experiment are plotted in figures 8(a) and (b), which show the relative phase difference plotted against channel position for targets having $k_\theta = 1.25\,\mathrm{cm}^{-1}$, $\Delta\phi \approx 1.3\pi$ and $k_\theta = 2.5\,\mathrm{cm}^{-1}$, $\Delta\phi \approx 0.7\pi$, respectively. Each plot also includes a best-fit line through the central eight channels, which produced the cleanest signals. In the case of figure 8(a), this represents $\sim 2\pi$ sampling of the poloidal corrugations, and in the case of figure 8(b), this represents $\sim 4\pi$ coverage (i.e. two full corrugation wavelengths). While the central eight channels were used to determine the poloidal wavenumber for the shorter wavelength corrugations, the full coverage of 16 channels will be required to resolve the longest poloidal wavelengths. Fortunately this is precisely the configuration (i.e. long wavelength corrugations, in which the reflectometry configuration reverts to the one-dimensional case), in which the outer eight channels should be the cleanest, enabling such measurements.

The horizontal bars in figure 8 represent the Gaussian width (in the poloidal direction) of each reflectometer channel, approximately 0.8 cm, which is the largest source of uncertainty in the linear fit, and can be considered the poloidal spatial resolution of the instrument. The measured k_θ values derived from figure 8 are $1.26 \pm 0.05\,\mathrm{cm}^{-1}$ and $2.49 \pm 0.09\,\mathrm{cm}^{-1}$, for corrugated targets of nominal wavenumbers $1.25\,\mathrm{cm}^{-1}$ and $2.5\,\mathrm{cm}^{-1}$, respectively. The slope of each data set recovers the poloidal wavenumber to well within the instrumental uncertainty.

4. Numerical simulation of laboratory results

In order to better understand the details of the target reflector measurements, the reflected field was analytically calculated using a solution to Maxwell's equations in cylindrical geometry.

Starting with the stationary wave equation for a linearly polarized wave

$$(\nabla^2 + k_0^2)\boldsymbol{E}(r,\theta) = 0, \tag{6}$$

where $\boldsymbol{E}$ is the electric field, $k_0 \equiv \omega n/c$ is the probing wavenumber, and n is the index of refraction, the general solution for the electric field is given by

$$\begin{aligned}\boldsymbol{E}(r,\theta) &= \hat{z}\,E_z(r,\theta)\\ &= \hat{z}\sum_{n=-\infty}^{\infty} C_n(J_n(k_0r) + \mathrm{i}Y_n(k_0r))\mathrm{e}^{\mathrm{i}n\theta},\end{aligned} \tag{7}$$

where J_n and Y_n are Bessel functions of the first and second kind, respectively, and C_n is the weighting coefficient for each Bessel component [16, 17].

The particular solution for a given configuration can be obtained by imposing a boundary condition at the wheel surface to determine the C_ns, corresponding to the illuminating beam and the wheel corrugations. The boundary condition can be defined in terms of Fourier components, as follows:

$$E_z(r_0,\theta) = \sum_{n=-\infty}^{\infty} a_n\mathrm{e}^{\mathrm{i}n\theta}, \tag{8}$$

where r_0 is the wheel radius and

$$a_n = \frac{1}{2\pi}\int_{-\pi}^{\pi} E_z(r_0,\theta)\mathrm{e}^{-\mathrm{i}n\theta}. \tag{9}$$

For the case of the laboratory target reflectors, the boundary condition can be explicitly defined by treating the surface as a sinusoidal phase perturbation to a Gaussian-shaped illumination intensity profile. Equation (9) can then be explicitly calculated using

$$E_z(r_0,\theta) = \mathrm{e}^{-(\theta/\Delta)^2}\mathrm{e}^{\mathrm{i}\phi}, \tag{10}$$

where Δ is the half-width of the illuminating Gaussian beam. Here,

$$\phi(\theta) = A\cos(p\theta + \theta_0), \tag{11}$$

where $p = k_\theta r_0$, $k_\theta = 2\pi/\lambda_{\mathrm{corr}}$, $A = 2\pi h_{\mathrm{corr}}/\lambda_0$, and θ_0 is the wheel rotation angle.

In the case of one-dimensional illumination, where the illuminating beam can be treated as spreading from a point source, an additional phase factor is introduced at the wheel surface due to the variation in the path length of the probing beam from the source to each position on the wheel. In this case, equation (11) is replaced with

$$\phi(\theta) = A\cos(p\theta + \theta_0) + \phi_{\mathrm{curv}}(\theta), \tag{12}$$

where

$$\phi_{\mathrm{curv}}(\theta) = k_0\sqrt{r_0^2\sin^2(\theta) + (d + r_0(1-\cos(\theta))^2} \tag{13}$$

and d is the distance between the source and closest point on the reflecting surface.

The full solution of the reflected complex electric field is then given by

$$E_z(r,\theta) = \sum_{n=-\infty}^{\infty} a_n\frac{(J_n(k_0r) + \mathrm{i}Y_n(k_0r))}{(J_n(k_0r_0) + \mathrm{i}Y_n(k_0r_0))}\mathrm{e}^{\mathrm{i}n\theta} \tag{14}$$

with the a_ns determined via equations (9)–(12).

Using this formulation for the reflected field, a direct comparison can be made between the simulated reflected field waveforms and the measured reflectometer signal, using the actual parameters from the laboratory set-up. Data from such a comparison are shown in figure 9, using the parameters of the first target wheel (i.e. data from figures 4(a) and (b)) with $k_\theta = 1.25\,\mathrm{cm}^{-1}$ and $h_{\mathrm{corr}} = 1.4\,\mathrm{mm}$. In the figure, the left-hand column contains output plots from the model (alternating amplitude and phase), and the right-hand column contains the corresponding laboratory measurements. Figures 9(a)–(d) represent $d = 10\,\mathrm{cm}$, figures 9(e)–(h) represent $d = 20\,\mathrm{cm}$, and figures 9(i)–(l) represent $d = 30\,\mathrm{cm}$.

The model represents the data quite accurately, even in the case at $d = 20\,\mathrm{cm}$, where the amplitude waveform is quite complicated and the phase waveform begins to exhibit visible distortion, and at $d = 30\,\mathrm{cm}$, where both the amplitude and phase waveforms are quite distorted due to interference effects. Even at the closest measurement, at $d = 10\,\mathrm{cm}$, the model precisely reproduces the amplitude modulations and the subtleties of the phase waveforms. It should be noted that it is not overly surprising that the model is accurate; one expects reliable analytical solutions to Maxwell's equations as long as the boundary conditions are correctly imposed.

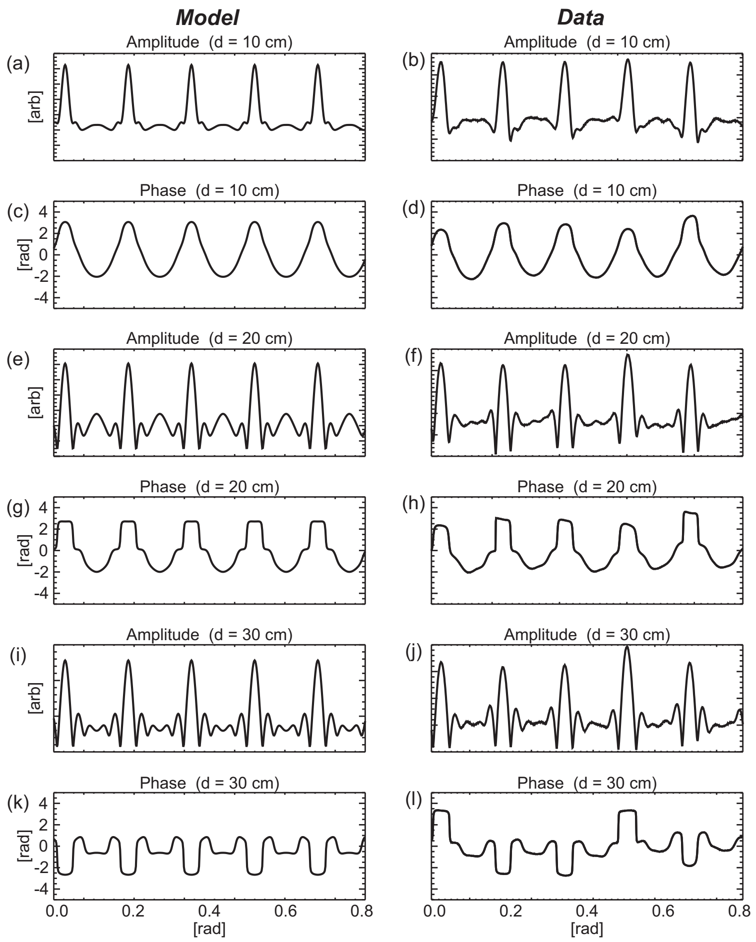

Figure 9. Comparison of model to laboratory waveforms for the one-dimensional system and the wheel shown in figure 4. The left-hand column contains output plots from the model (alternating amplitude and phase), and the right-hand column contains the corresponding laboratory measurements. (a)–(d) represent $d = 10\,\mathrm{cm}$, (e)–(h) represent $d = 20\,\mathrm{cm}$, and (i)–(l) represent $d = 30\,\mathrm{cm}$.

That said, it is critical to establish that the complicated waveforms measured with the one-dimensional system are indeed a fundamental product of the interference from the corrugations on the target, and not merely a spurious experimental artefact.

One interesting difference between the model and the data can be seen in figures 9(*k*) and (*l*). Here, the data match the model for certain intervals, but appear to more closely match plot (*g*) for other intervals. By looking at the corresponding amplitude waveform, it can be seen that the high-harmonic 'dropouts' in the phase waveform appear between points where the amplitude drops to near zero, and there is a fundamental ambiguity in the subsequent phase interpretation. The small nonuniformities in the target wheel construction can therefore have a dramatic effect on the reconstruction of the phase. These should not be interpreted as merely spurious 'phase jumps' which can be removed or corrected, but rather a fundamentally ambiguous result of destructive wave interference. As will be seen in figure 12, the complication of additional modes makes it nearly impossible to positively identify the location of the phase ambiguities for waveforms exhibiting strong interference effects.

It should be reiterated that the reconstruction of the details of the phase waveform for these cases is only possible by knowing the exact shape of the reflecting surface beforehand. Additionally, each of the cases studied contains only a single, clean mode. The addition of additional modes or a realistic k_θ spectrum further complicates the resulting waveforms. These situations are specifically addressed at the end of this section (for two modes) and in section 5 (for a realistic spectrum of modes).

The broad implication from the target wheel tests is that for sufficiently low k_θ and h_{corr}, imaging is unnecessary and one-dimensional reflectometry can be expected to produce valid fluctuation measurements. If either (or both) of these quantities is increased, however, the degradation of the signal quality due to wave interference becomes an important consideration. It is interesting, then, to use the formulation from equation (14) to explore the dependences of the wavefield on these two parameters.

Figures 10(*a*)–(*c*) show the modelled reflected field amplitude from a target having $k_\theta = 1.25\,\mathrm{cm}^{-1}$ and $h_{\mathrm{corr}} = \lambda_0/8, \lambda_0/2$, and λ_0 ($\Delta\phi = 0.5\pi$, 2π, and 4π, respectively). Figure 10(*b*) also shows, drawn to scale, the collection solid angle of the MIR system compared to that of a typical one-dimensional detection horn. In the figure, the corrugated wheel surfaces are also drawn to scale.

In the case with the lowest corrugation amplitude (figure 10(*a*)), clear striations are visible due to the focusing effect of each concave region of the target. Even at the right-most edge of the simulation space (at $d = 50\,\mathrm{cm}$), the degree of amplitude modulation is relatively low, and, though not shown in the figure, the phase measurement is generally intact. As the corrugation amplitude increases, however, the amplitude modulations are more pronounced, and higher order harmonics of the corrugations are visible in the field pattern. In figure 10(*c*), the interference patterns are quite intricate, including several harmonic orders, even quite close to (within $\sim$10 cm of) the reflecting surface. As was seen in the target wheel tests and in figure 9, the phase waveforms in these cases become distorted and ambiguous.

Similarly to the parameter scan of h_{corr} at constant k_θ shown in figure 10, it is informative to perform a parameter scan of k_θ at constant h_{corr}. Figures 11(*a*)–(*c*) show the modelled reflected field amplitude from a wheel having $h_{\mathrm{corr}} = \lambda_0/2$ ($\Delta\phi = 2\pi$), and $k_\theta = 0.5\,\mathrm{cm}^{-1}$, $1.0\,\mathrm{cm}^{-1}$, and $2.0\,\mathrm{cm}^{-1}$, respectively. As in figure 10 and 11(*b*), figure 11(*b*) also shows the collection solid angle of the MIR and one-dimensional configurations.

For the case with lowest k_θ (figure 11(*a*)), there are only minor focusing effects on the reflected field intensity, which leaves the phase information intact. As k_θ increases to 1–2 cm^{-1}, however, the field mapping becomes extremely complicated, exhibiting a multitude of harmonic orders, even in the close vicinity of the reflecting surface.

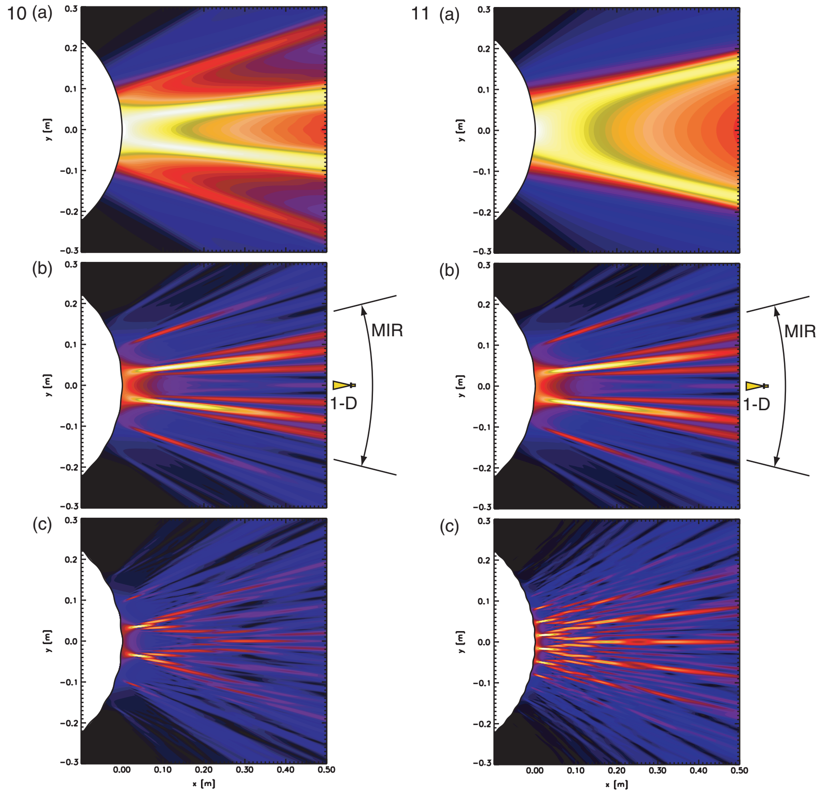

Figures 10 and 11. (10) Parameter scan of $h_{\mathrm{corr}}(\Delta\phi)$ at constant k_θ. Modelled reflected field amplitude from a target having $k_\theta = 1.25\,\mathrm{cm}^{-1}$ and $\Delta\phi = 0.5\pi$, 2π, and 4π, respectively. Also shown is the collection solid angle of the MIR system compared to that of a typical one-dimensional detection horn. The corrugated wheel surfaces are also drawn to scale. (11) Parameter scan of k_θ at constant $h_{\mathrm{corr}}(\Delta\phi)$. Modelled reflected field amplitude from a target having $\Delta\phi = 2\pi$, and $k_\theta = 0.5\,\mathrm{cm}^{-1}$, $1.0\,\mathrm{cm}^{-1}$, and $2.0\,\mathrm{cm}^{-1}$, respectively.

Again, the complexity of these field patterns, when sampled at field points located 10, 20, and 30 cm from the reflecting surface and simulated as a function of wheel rotation angle to produce a modelled waveform, precisely match the actual waveforms measured in the laboratory, as shown in figure 9.

An important point to consider when comparing the target reflector tests to a more realistic plasma turbulence scenario is the effect of multiple k_θ modes on the collected phase information. The intention of the target reflector tests was to investigate the effect of interference on reflectometer signals in the simplest manner possible, and therefore the corrugation patterns on each reflector were intended to contain a relatively pure single k_θ value. However, due to construction irregularities, even the supposedly 'monochromatic' targets contained additional spectral components. This can be seen in figures 4 and 7, which contain small deviations from exact sinusoids.

In the case of figure 4, the additional spectral components cause a breaking of the symmetry of the waveform in the one-dimensional configuration (figure 4(b)), while the waveform is precisely reproduced in the MIR case, including the amplitude variations among individual oscillation periods (figure 4(c)).

The case of figure 7 is investigated here. Figure 12(*a*) shows the modelled waveform from a target reflector of $k_\theta = 2.5\,\mathrm{cm}^{-1}$ and $\Delta\phi \approx 0.7\pi$, recorded with the detector at a distance of $d = 25\,\mathrm{cm}$. This is exactly the configuration of the laboratory measurements shown in figure 7(*b*). The grey curve in figure 12(*a*) represents the corrugations at the reflector, and the black curve represents the modelled phase at the detector.

Similarly to the previous examples, the modelled waveform in figure 12(*a*) is a close match to the periodic section of the corresponding data in figure 7(*b*), however the data exhibits multiple phase jumps/ambiguities which do not appear in the single-mode model.

The power spectra for the detected and reference waveforms is shown in figure 12(*b*). Immediately noticeable in the power spectrum are the appearance of multiple harmonic orders, with the second harmonic approaching the power level of the fundamental. The interference pattern is quite periodic, however, due to the exact periodicity of the reflector, and as a result each harmonic order in the power spectrum is relatively clean and distinct from the others.

Figure 12(*c*) shows the result of adding a single additional k_θ component, at a level of 40% of the original mode. Again, the grey curve is the corrugation pattern on the target reflector (i.e. the one-dimensional phase pattern), and the black curve is the simulated measurement at $d = 25\,\mathrm{cm}$. Because the precise periodicity of the reflector is now broken, the quasi-periodicity of the interference pattern disappears. The data from figure 7(*b*) is most closely represented by figure 12(*c*), complete with random phase-jumps.

A relatively small change in the shape of the reflector (even while keeping the average phase deviation $\sqrt{\langle(\Delta\phi)^2\rangle}$ at the wheel surface virtually unchanged) results in a dramatic change in the detected interference pattern, which has become relatively chaotic. This is corroborated by figure 12(*d*), which shows the power spectra of the reflector and the detected signal for this case. The addition of the second k_θ component is clearly visible on the grey reference curve, while the black measurement curve has become almost noise-like.

This example serves to demonstrate that in the cases where interference plays a significant role, modelling the effect of interference by looking at a single k_θ mode can be overly optimistic. Even in cases where a single mode produces an interference pattern which appears to be

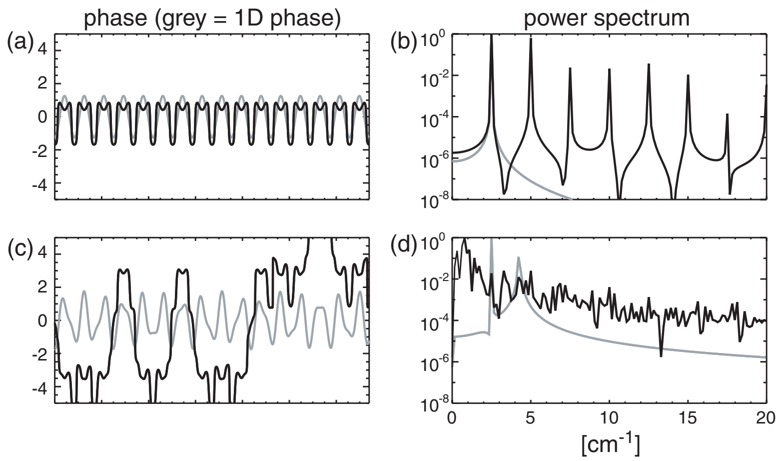

Figure 12. (*a*) Modelled waveform from a target with $k_\theta = 2.5\,\mathrm{cm}^{-1}$ and $\Delta\phi = 0.7\pi$ (i.e. figure 7(*b*)), measured at the target surface (grey curve) and at $d = 25\,\mathrm{cm}$ (black curve). (*b*) Corresponding power spectra. (*c*) Modelled waveform from a target with an additional k_θ component, at a level of 40% of the original mode, at the target surface and at $d = 25\,\mathrm{cm}$. (*d*) Corresponding power spectra.

quasi-periodic and only contain relatively clean higher harmonics, the addition of even a single additional k_θ component can destroy the signal behaviour, and thus the ability to infer the characteristics of the reflecting surface based on the detected signal. At the same time, any direct quantitative comparison of absolute fluctuation levels between the target-reflector tests and realistic plasma conditions is necessarily imprecise, since in the former case nearly all of the spectral energy is in a single mode, and in the latter case the energy is spread over the k_θ spectrum.

It should also be noted that, while the TEXTOR instrument is configured for extraordinary mode (X-mode) polarization, the effects of interference and the implications of optically focusing the radiation with a MIR instrument are equally valid for ordinary mode (O-mode) polarization.

5. Implications of MIR on correlation length determination

One of the most interesting uses of reflectometry for fluctuation measurements in plasmas is that of correlation reflectometry, in which measurements are made at multiple locations, enabling a map of cross-correlations between adjacent points to be used to derive a turbulence correlation length [18]. Previously, this type of measurement has been performed using multiple probing frequencies to probe closely spaced cutoff layers and derive radial correlation lengths.

While the use of imaging reflectometry, which provides localized poloidal measurements, extends the applicability of correlation reflectometry to the poloidal direction, it also has a direct implication for the measurement of radial correlation lengths.

As introduced in section 1, the interpretation of cross-correlation factors between signals from one-dimensional reflectometers can be quite difficult. It has been demonstrated that the correlation length of the measured signals needs to be 'corrected' to retrieve the correlation length of the turbulence [1, 5, 6], with various techniques employed. These correction factors generally depend on the poloidal wavenumber spectrum or the magnitude of the fluctuations, and can become nonlinear or even inapplicable as the level of turbulence increases.

With the use of imaging reflectometry, this difficulty is removed; each detector measures the true fluctuation phase, and the signal correlation length directly provides the correlation length of the fluctuations. This simplifies the interpretation of radial correlation lengths and, with the use of an array of detectors, provides poloidal correlation lengths as well.

6. Discussion

The laboratory results presented here serve two primary purposes; to characterize the TEXTOR instrument in advance of actual tokamak experiments, and to experimentally explore the fundamentals of two-dimensional effects on reflectometry measurements in a controlled manner. In short, the results demonstrate the circumstances which impose a limitation on the interpretation of standard reflectometry, and the recovery of the measurements using imaging techniques.

Target reflectors with poloidal wavenumbers of $k_\theta = 1.25$–$2.5\,\mathrm{cm}^{-1}$ and corrugation amplitudes of $\Delta\phi \approx 0.7\pi$–$2\pi$ were tested using both a conventional reflectometry configuration and the MIR configuration. It was found that for the longer wavelength, lower amplitude target, both the one-dimensional and MIR configurations were able to accurately measure the target surface, out to measurement distances on the order of 1 m (i.e. distances typically accessible to plasma diagnostics). For the shorter wavelength and/or higher amplitude corrugations, the one-dimensional configuration was able to accurately measure the surface at very close proximity, but the signal was effectively destroyed as the measurement distance was increased beyond 20–30 cm. The MIR configuration was able to recover the measurement when the target was located in the focal region, but suffered similar destruction of the signal as the target was moved beyond a ± 10 cm depth-of-field. In short, the MIR configuration tranferred the 'proximity focusing' of the one-dimensional system to a remote focal plane (235 cm from the target), which represents a distance readily accessible to diagnostics on plasma devices.

Results from both single-point and multipoint (poloidally distributed) measurements are presented. These demonstrate the significance of large aperture optics for even single measurements, as well as the additional information obtainable with a poloidal array.

The testing scenario was modelled using a two-dimensional solution to Maxwell's equations, with all boundary conditions and wave parameters chosen to match the geometry of the experimental set-up (i.e. no arbitrary 'calibration' factors). The simulation provided an extremely close match to the experimental results, and served to verify that the target-mirror test data indeed demonstrate a fundamental consequence of wave interference. The model was also used to provide a simple illustration of the dependences of the interference complexity on the two fundamental fluctuation parameters k_θ and $\Delta\phi$ via parameter scans over values relevant to ITG turbulence measurements.

It is important to reiterate that the studies presented here represent a simpler scenario than actual plasma measurements, which include finite refraction effects, particularly near the cutoff. The modelling results of section 4 were configured to best represent the laboratory tests, which of course do not include plasma effects. Such an approximation, generally called the 'phase-screen' model of reflection from rough surfaces, accurately describes the laboratory tests, and has direct relevance to plasma measurements through the existence of the virtual cutoff (see section 1).

The set of experiments presented here provide a guideline for the interpretation of data with the MIR instrument. Namely, this instrument has been designed with the presumption that optical imaging of the virtual cutoff layer in a plasma will enable localized sampling of this surface, and will greatly reduce the effects of interference introduced by two-dimensional fluctuations. While the experiments presented here have not proved or disproved that presumption, they have verified that the instrument does indeed accomplish the goal of imaging the reflection layer.

With this in mind, it is important to recall that detailed modelling of reflectometry including full-wave solutions to Maxwell's equations, plasma refraction, realistic spectra of turbulent modes, and complete two-dimensional effects, have been previously published in [3, 7], and have indeed guided the development of the MIR technique. The results from these detailed numerical studies, originally performed for plane waves in planar geometry, were later verified for Gaussian beams in cylindrical geometry.

Both the results from the target wheel studies as well as the previous detailed numerical work bear out the strong dependences of reflectometer data on the two quantities k_θ and $\Delta\phi$, consistent with the expression for the diffraction distance from a phase-grating [3], defined as $D_{\mathrm{diff}} \approx 2k_0/[(1+\sigma_\phi^2)\Delta k_\theta^2]$, where $\sigma_\phi \approx \sqrt{\langle(\Delta\phi)^2\rangle}$ and Δk_θ is the width of the poloidal mode spectrum. As a rough guide, one can expect interference to play a significant role in the reflected field pattern if measurements are taken beyond D_{diff}.

It is also worth mentioning a particular previous study on this subject, in which correlation length measurements taken with a conventional reflectometer were compared with Langmuir probe measurements in the edge of the LAPD linear device [19]. In this paper, close agreement was found between the probe array and the one-dimensional reflectometer results. While this study has occasionally been used (mistakenly) as an example to demonstrate the absence of two-dimensional effects on reflectometry measurements, in fact the author specifically states that these measurements were taken within the diffraction distance, and therefore do not address the validity of conventional reflectometer measurements in the presence of two-dimensional interference [20].

Similarly, reflectometric measurements of long-wavelength fluctuations such as MHD phenomena, with poloidal wavenumber $k_\theta \ll 1$, will fall well within the one-dimensional approximation, and are expected to be unaffected by the two-dimensional interference effects addressed here.

Acknowledgments

The authors would like to thank the TEXTOR team for their continuing support of this project. This work was supported by US DOE contracts DE-AC02-76CH03073, DE-FG02-99ER54523 and the US DOE Fusion Energy Postdoctoral Fellowship.

References

[1] Mazzucato E and Nazikian R 1993 *Phys. Rev. Lett.* **71** 1840
[2] Nazikian R and Mazzucato E 1995 *Rev. Sci. Instrum.* **66** 392
[3] Mazzucato E 1998 *Rev. Sci. Instrum.* **69** 1691
[4] Mazzucato E *et al* 1996 *Phys. Rev. Lett.* **77** 3145
[5] Conway G D 1997 *Plasma Phys. Control. Fusion* **39** 407
[6] Nazikian R 1997 *J. Mod. Opt.* **44** 1037
[7] Mazzucato E 2001 *Nucl. Fusion* **41** 203
[8] Mazzucato E *et al* 2002 *Phys. Plasmas* **9** 1955
[9] Munsat T *et al* 2003 *Rev. Sci. Instrum.* **74** 1426
[10] Deng B H, Domier C W, Luhmann Jr N C, Brower D L, Donné A J H, Oyevaar T and van de Pol M J 2001 *Phys. Plasmas* **8** 2163
[11] Conway G D, Schott L and Hirose A 1996 *Rev. Sci. Instrum.* **67** 3861
[12] Pavlichenko O S, Skibenko A I, Fomin I P, Pinos I B, Ocheretenko V L and Berezhniy V L 2001 *Proc. 5th Int. Workshop on Reflectometry* ed K Kawahata (National Institute for Fusion Science, Oroshi-cho, Toki 509-5292, Japan, 2001) No NIFS-PROC-49, p 85
[13] Conway G D 1993 *Rev. Sci. Instrum.* **64** 2782
[14] Leica Geosystems A G, Mönchmattweg 5 CH-5035 Unterentfelden, Switzerland www.leica-geosystems.com
[15] Bendat J S and Piersol A G 2000 *Random Data: Analysis and Measurement Procedures* 3rd edn (New York: Wiley) *Appendix B: Definitions for Random Data Analysis*
[16] Budden K G 1985 *The Propagation of Radio Waves* (Cambridge: Cambridge University Press)
[17] Harrington R F 1961 *Time-Harmonic Electromagnetic Fields* (New York: McGraw-Hill)
[18] Costley A E, Cripwell P, Prentice R and Sips A C C 1990 *Rev. Sci. Instrum.* **61** 2823
[19] Gilmore M, Peebles W A and Nguyen X V 2000 *Plasma Phys. Control. Fusion* **42** L1
[20] Gilmore M A 1999 *PhD Thesis* UCLA